Anharmonic thermo-elasticity of tungsten from accelerated Bayesian adaptive biasing force calculations with data-driven force fields

Anruo Zhong,[*] Clovis Lapointe, Alexandra M. Goryaeva ⬤, Jacopo Baima, Manuel Athènes ⬤,[†] and Mihai-Cosmin Marinica ⬤[‡]

Université Paris-Saclay, CEA, Service de Recherche en Corrosion et Comportement des Matériaux, SRMP, 91191 Gif-sur-Yvette, France

The elastic properties of tungsten, a ubiquitous material in future energy systems, are investigated up to its melting temperature by means of a data-driven approach. The proposed workflow combines machine learning of the force field and enhanced sampling of the crystalline structure. While the machine learning force field achieves the accuracy of *ab initio* calculations, its implementation in sampling methods is often limited due to its high computational cost, which is commonly a few orders of magnitude larger than that of traditional potentials. To overcome this limitation, we propose a fast and robust Bayesian sampling scheme aiming at estimating the fully anharmonic free energy of crystalline solids with the help of an improved adaptive biasing force method. This method performs a thermodynamic integration from a harmonic reference system, wherein zero frequencies associated with the periodic boundaries are screened off. The proposed sampling method drastically improves the speed of convergence and overall accuracy. We demonstrate the efficiency of the improved method by calculating the second order derivatives of the free energy, such as the elastic constants, which are performed almost 100 times faster than with the standard methods. The proposed method enables the prediction of the elastic properties of tungsten in the range of temperatures that cannot be investigated experimentally, from 2100 K to the melting temperature. The accuracy and numerical efficiency of the proposed strategy open up many avenues for the reliable prediction of finite-temperature properties of materials, such as the relative stability of structural defects and elastic constants.

I. INTRODUCTION

The thermodynamic properties of materials, such as heat capacity, thermoelasticity, and phase stability, are crucial benchmarks in materials design, as they determine the performance and practical applications of a given material. This knowledge is therefore essential to understand the behavior at finite temperature of new materials. Experimental measurements of the thermal quantities are often time consuming, expensive, or even unfeasible under extreme conditions, e.g., at high temperatures and/or pressures. Atomic-scale simulations are therefore widely used to predict the thermodynamic quantities of practical interest and/or extrapolate them beyond experimental conditions.

Thermodynamic properties are well characterized by the free energy and its derivatives. In crystalline solids, an accurate representation of the free energy includes three contributions: (i) the contribution accounting for chemical disorder and including configurational entropy, which can be computed using Monte Carlo simulations or approximated assuming that the lattice is rigid, (ii) the contribution of the electronic excitations, and (iii) the harmonic and anharmonic contributions of the lattice vibrations, i.e., the interactions of phonons with themselves and with other modes of excitation. In this paper, we consider pure chemical systems whose configurational entropy is equal to zero and we do not implement any special treatment for the electronic free energy. We thus focus on the vibrational contribution to free energy. Its harmonic part can be straightforwardly obtained by computing the phonon spectrum resorting to the harmonic or quasiharmonic approximations [1–3]. These two approximations however become inaccurate at elevated temperatures for which phonon softening and broadening should be accounted for [4]. Recently, Swinburne *et al.* introduced an analytical mean-force model able to directly compute the anharmonic free energy of a general bond lattice within meV/atom accuracy [5]. Although computationally inexpensive, this model is restricted to perfect crystals and difficult to extend in presence of imperfections.

The anharmonic free energy contribution, which is crucial for deriving the high-temperature properties, can be directly evaluated by thermodynamic integration (TI) from a suitable reference system [2,6,7]. In TI, the first derivative of free energy is first estimated using a sampling algorithm and then integrated. TI-based calculations of thermodynamic properties including the effect of anharmonicity from accurate electronic structure calculations, i.e., *ab initio* calculations, were initiated in 2001 [8,9].

Such a brute-force integration is often computationally prohibitive in practice, e.g., in electronic structure calculations, as it requires one to sample too many configurations

---

[*]anruo.zhong@cea.fr
[†]manuel.athenes@cea.fr
[‡]mihai-cosmin.marinica@cea.fr

along the path of integration [10]. Therefore, several improvements have been proposed to make TI-based methods more feasible and amenable to electronic structure calculations in particular. Notably, upsampled thermodynamic integration using Langevin dynamics (UP-TILD) method was developed [11], which enhances the performance of TI by combining the density functional theory (DFT) calculations using "reduced" DFT parameters (energy cutoff of kinetic energy and k-points sampling of the Brillouin zone) with an almost configuration-independent offset with respect to the fully converged energy, where only a small number of configurations are required to evaluate the fully converged term. Based on UP-TILD, an improved version, referred to as two-stage upsampled thermodynamic integration using Langevin dynamics (TU-TILD), was developed to further accelerate the convergence of the calculation [12], wherein TI is split into two stages, first from the harmonic to an intermediate potential, and then from the intermediate potential to the exact DFT Hamiltonian. The TU-TILD scheme has recently been applied with moment tensor potentials (MTPs) [13], a class of machine learning (ML) potentials which has demonstrated accuracy and efficiency [10,14,15]. However, these approaches assume that the points sampled from the reference distribution faithfully represent the target distribution associated with the exact Hamiltonian. This assumption can be true for high quality reference or intermediate potentials, such as the MTPs within the ML framework, but is not very reliable when using simple reference systems such as harmonic or quasiharmonic Hamiltonians [10]. Generally speaking, when ML potentials are chosen as intermediate potential, the free energy from the reference should be computed with great accuracy. However, this can be a crude task because, at least for crystalline materials, the ML force fields are from a few tens times slower up to four orders of magnitude slower in terms of CPU times than, for instance, traditional embedded-atom-method (EAM) potentials. The developments proposed below aim precisely at reducing the computational costs: We present a method for fast evaluation of the anharmonic free energy employing numerically heavy force fields without assuming that sampling the relevant configurations from the reference distribution is equivalent to sampling from the target distribution associated with the exact Hamiltonian.

Our method mixes the reference and target Hamiltonian states, and recovers the correct statistics resorting to the Bayes formula, without any approximation. It builds on the free energy perturbation (FEP) method [16] and adaptive sampling approach [17–25]. The FEP method consists of sampling the reference distribution and estimating the free energy difference via the logarithm of a partition function ratio [16]. In practice, the accuracy of the FEP method is controlled by the degree of overlap between the reference and target distributions [26]. Sampling from another distribution exhibiting better overlapping properties with both the target and reference distributions usually improves the accuracy. This importance-sampling approach for the calculation of free energy difference traditionally employs an auxiliary biasing potential and is dubbed umbrella sampling [27,28], precisely because the sampling distribution specified by the biasing potential should cover simultaneously the region of configuration space relevant to both the target and reference systems.
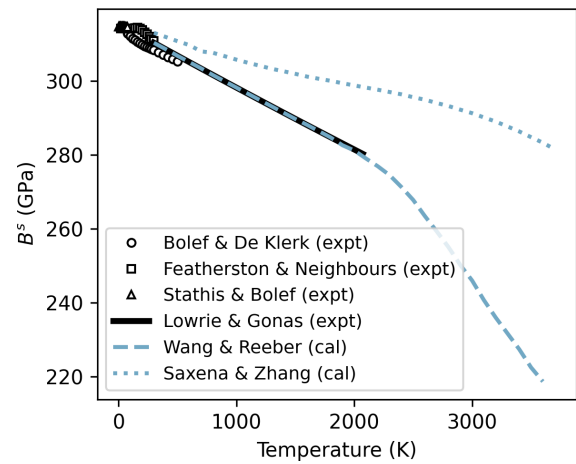

FIG. 1. Adiabatic bulk modulus B^S of W. Experimental values are obtained from four different experiments in the temperature range from 4.2 to 2 073.15 K [49–52], while the calculated values are extended up to the melting point by two models [53,54].

Establishing such a biasing potential that provides good overlapping properties is a challenging task. Here, we propose to construct the biasing potential adaptively by averaging and integrating the derivative of the extended Hamiltonian with respect to the mixing (coupling) parameter, using the adaptive biasing force (ABF) method [17,18,29–31] and a Bayesian reasoning framework [32–35]. ABF-based techniques have been widely developed and applied over the past two decades [36–41]. It is rigorously proved that the biasing force in ABF method converges to the free energy in the long time limit [42]. The Bayesian formulation for the extended Hamiltonian allows one to systematically reduce the statistical variance of the estimated free energy difference when the converged biasing force is frozen, compared with the other standard estimators (FEP, TI, thermodynamic-occupation, and weighted-histogram estimators; refer to Ref. [34]). Note that this Bayesian approach can be viewed as a particular and efficient FEP method because the biasing mean force is computed through umbrella sampling and because the implemented Bayes formula corresponds to a FEP equation in which the sampled reference distribution is a biased marginal probability distribution.

Here, a Bayesian adaptive approach is used to compute the anharmonic free energy of a crystalline solid. In this paper, we enrich the Bayesian adaptive approach with two new features: We eliminate the numerical instabilities of the reference Hamiltonian via a singular value decomposition (SVD) filter to increase the sampling robustness, and we introduce a simple weighting scheme for the biasing force to enhance the initial speed of convergence.

Beyond the methodological aspects, our main application concerns the crystalline tungsten (W), which has been selected as potential material of choice in plasma facing components such as the divertor of fusion reactors due to its high melting point [43,44]. Despite this huge industrial interest for W, its high-temperature mechanical properties remain perplexing. As presented in Fig. 1, there is no direct measurement of elastic constants of the body centered cubic (bcc) phase of

W for temperatures higher than 2100 K, while numerical calculations of a system at such temperatures suffer severe statistical fluctuations.

.Although the ML force fields approach the accuracy of *ab initio* calculations [45–48], their applications for free energy calculation are often limited due to their high computational cost. To address this issue, we use the fast and robust Bayesian scheme mentioned above to estimate the fully anharmonic free energy of crystalline solids, providing access to the exact thermodynamic properties, even those derived from the second derivatives of the free energy, up to the melting point with *ab initio* accuracy. This approach is validated by the calculations of thermodynamic properties of W, in comparison to the experimental results at temperatures below 2100 K and to the traditional molecular dynamics (MD) simulations at temperatures above 2100 K. With sufficient efficiency to apply the ML potentials, this accelerated ABF method makes the fast and accurate investigation of free energy at extremely high temperatures feasible.

The paper is organized as follows. In Sec. II, we detail and validate the method, including the theoretical framework, algorithm implementation, and optimizations concerning the reference system for TI and the weighting function for sampling. In Sec. III, we present the thermodynamic properties of W computed with this method, using traditional EAM potentials as well as existing and newly constructed ML potentials. A polynomial model of high-temperature properties for W is proposed.

II. METHODS OF FREE ENERGY CALCULATION

Calculating the anharmonic free energy is a challenging task as explained above. It is only possible to compute the absolute Helmholtz free energy of a few relatively simple material models (e.g., harmonic solids) which therefore play the role of reference system. To obtain thermodynamic properties of crystalline materials, the important quantity to compute is actually the difference in free energy between the target crystalline system and a reference solid. We explain below in detail the theoretical framework, the proposed methodological improvements, and the numerical implementation schemes which make it possible to compute the anharmonic contribution as a free energy difference.

A. Calculation of free energy difference using thermodynamic integration

For a system with N_a atoms, the thermodynamic integration is performed using a general potential energy $U(\zeta, \mathbf{r})$ that linearly mixes the potential energy of the given target system $U(\mathbf{r})$ and of the reference system $U_{\text{ref}}(\mathbf{r})$ through a coupling parameter ζ:

$$U(\zeta, \mathbf{r}) = \zeta U(\mathbf{r}) + (1 - \zeta)U_{\text{ref}}(\mathbf{r}), \quad (1)$$

where $\mathbf{r}$ is the set of positions of N_a atoms defined in the $3N_a$-dimensional torus $\mathbb{T}^{3N_a} \subset \mathbb{R}^{3N_a}$ (the configuration space with periodic boundary conditions). Here, the coupling parameter ζ, similar to a reaction coordinate, has real values inside the [0,1] range. This interval will be discretized in practice into 201 equally spaced discrete values. Beyond this

simple numerical setup, some strategies have proven useful in variance minimization and convergence acceleration, including adoption of a nonlinear dependence of the potential on the coupling parameter [16], as well as modification of discretization method [55]. Besides, the free energy difference can be directly computed from a single very long simulation in which the temporal reaction coordinate $\zeta(t)$ progresses linearly from 0 to 1 [56]. Although sometimes advantageous, it is unnecessary to employ such methods in our case for which accuracy and efficiency are both guaranteed by the Bayesian formalism.

The corresponding partition function for the canonical ensemble can be further derived:

$$Z(N_a, V, T, \zeta) = \frac{1}{\Lambda^{3N_a} N_a!} \int_{\mathbb{T}^{3N_a}} \exp\left[-\beta U(\zeta, \mathbf{r})\right] d\mathbf{r}, \quad (2)$$

where Λ is de Broglie thermal wavelength and $\beta = 1/(k_B T)$ with k_B the Boltzmann constant and T the temperature. This partition function gives access to the probability of finding the generalized system in a state characterized by ζ:

$$P_0(\zeta) = \frac{Z(N_a, V, T, \zeta)}{\int_0^1 Z(N_a, V, T, \tilde{\zeta}) d\tilde{\zeta}}. \quad (3)$$

The associated Landau free energy is defined as

$$A(\zeta) = -\beta^{-1} \ln P_0(\zeta) \quad (4)$$

$$= -\beta^{-1} \ln Z(N_a, V, T, \zeta) + B, \quad (5)$$

where the quantity B is independent of ζ. Then, the derivative of the free energy can be deduced:

$$A'(\zeta) = \frac{\int_{\mathbb{T}^{3N_a}} \partial_\zeta U(\zeta, \mathbf{r}) \exp\left[-\beta U(\zeta, \mathbf{r})\right] d\mathbf{r}}{\int_{\mathbb{T}^{3N_a}} \exp\left[-\beta U(\zeta, \mathbf{r})\right] d\mathbf{r}}$$

$$= \left\langle \frac{\partial U(\zeta, \mathbf{r})}{\partial \zeta} \right\rangle_\zeta, \quad (6)$$

where $\langle \cdot \rangle_\zeta$ denotes the ensemble average. Integration of Eq. (6) between $\zeta = 0$ and 1 gives the difference in free energy:

$$\Delta A = A(1) - A(0) = \int_0^1 \langle U(\mathbf{r}) - U_{\text{ref}}(\mathbf{r}) \rangle_\zeta d\zeta, \quad (7)$$

where $A(0)$ and $A(1)$ are the free energy, respectively, associated to the reference potential $U_{\text{ref}}(\mathbf{r})$ and the potential energy $U(\mathbf{r})$. Based on Eq. (7), determination of free energy of any given system is subject to two requirements: The existence of a reference system for which free energy can be calculated numerically or analytically, as well as a reversible artificial pathway between the system of interest and the reference crystal, which allows one to carry out the thermodynamic integration of potential energy. Here the coupling parameter ζ provides a smooth transition from a known reference state to a realistic system.

To numerically calculate the integral in Eq. (7), we propose an optimized ABF algorithm based on the previous Bayesian ABF (BABF) approach [32].

B. Bayesian adaptive biasing force

The main motivation for the development of the ABF method is to overcome the obstacles arising during the ther-

modynamic integration due to free energy barriers [16,55]. As an alternative of MD and Monte Carlo simulations with proven convergence [42], the ABF algorithm improves remarkably the sampling efficiency [17,18,29–31]. In this method, a bias is added directly to the forces acting on the atoms, counteracting the mean force along the transition direction to prevent the system from being trapped by the free energy barrier, as well as reducing the statistical variance [34]. We consider the corresponding biasing potential $U_{A_\star}(\zeta, \mathbf{r})$ defined as

$$U_{A_\star}(\zeta, \mathbf{r}) = U(\zeta, \mathbf{r}) - A_\star(\zeta), \tag{8}$$

where $A_\star$ is the biasing potential added to the extended potential. Let $P_{A_\star}(\zeta, \mathbf{r})$ denote the joint probability of the extended state $(\zeta, \mathbf{r})$ in the extended ensemble with biasing potential $A_\star$. We have

$$P_{A_\star}(\zeta, \mathbf{r}) = \frac{\exp\left[-\beta U_{A_\star}(\zeta, \mathbf{r})\right]}{\iint_{\mathbb{T}^{3N_a} \times [0,1]} \exp\left[-\beta U_{A_\star}(\tilde{\zeta}, \tilde{\mathbf{r}})\right] d\tilde{\zeta} d\tilde{\mathbf{r}}}. \tag{9}$$

Then the mean force $A'(\zeta)$ formalized by Eq. (6) can be transposed in the extended ensemble associated with the biasing potential $U_{A_\star}(\zeta, \mathbf{r})$:

$$A'(\zeta) = \frac{\int_{\mathbb{T}^{3N_a}} \partial_\zeta U(\zeta, \mathbf{r}) \exp[-\beta U_{A_\star}(\zeta, \mathbf{r})] d\mathbf{r}}{\int_{\mathbb{T}^{3N_a}} \exp[-\beta U_{A_\star}(\zeta, \mathbf{r})] d\mathbf{r}}$$
$$= \frac{\int_{\mathbb{T}^{3N_a}} \partial_\zeta U(\zeta, \mathbf{r}) P_{A_\star}(\zeta, \mathbf{r}) d\mathbf{r}}{\int_{\mathbb{T}^{3N_a}} P_{A_\star}(\zeta, \mathbf{r}) d\mathbf{r}}. \tag{10}$$

The above equality indicates that it is possible to compute the mean force in the biased extended system. We show how to do it through Bayesian reasoning.

The marginal probability of ζ and $\mathbf{r}$ can be expressed as $P_{A_\star}(\zeta) = \int_{\mathbb{T}^{3N_a}} P_{A_\star}(\zeta, \mathbf{r}) d\mathbf{r}$ and $P_{A_\star}(\mathbf{r}) = \int_0^1 P_{A_\star}(\zeta, \mathbf{r}) d\zeta$, respectively. Then, the conditional probability of ζ for a given $\mathbf{r}$ is given by $p_{A_\star}(\zeta|\mathbf{r}) = P_{A_\star}(\zeta, \mathbf{r})/P_{A_\star}(\mathbf{r})$ while that of $\mathbf{r}$ for a given ζ is $p_{A_\star}(\mathbf{r}|\zeta) = P_{A_\star}(\zeta, \mathbf{r})/P_{A_\star}(\zeta)$. The two equivalent expressions of the joint probability below

$$p_{A_\star}(\mathbf{r}|\zeta) P_{A_\star}(\zeta) = p_{A_\star}(\zeta|\mathbf{r}) P_{A_\star}(\mathbf{r}) \tag{11}$$

allow one to formulate the Bayes relation, expressing the conditional probability of $\mathbf{r}$ given ζ as a function of that of ζ given $\mathbf{r}$:

$$p_{A_\star}(\mathbf{r}|\zeta) = \frac{p_{A_\star}(\zeta|\mathbf{r}) P_{A_\star}(\mathbf{r})}{P_{A_\star}(\zeta)}. \tag{12}$$

The two equivalent expressions in Eq. (11) also allow one to cast the mean force in Eq. (10) into the two respective forms:

$$A'(\zeta) = \int_{\mathbb{T}^{3N_a}} \partial_\zeta U(\zeta, \mathbf{r}) p_{A_\star}(\mathbf{r}|\zeta) d\mathbf{r} \tag{13}$$
$$= \frac{\int_{\mathbb{T}^{3N_a}} \partial_\zeta U(\zeta, \mathbf{r}) p_{A_\star}(\zeta|\mathbf{r}) P_{A_\star}(\mathbf{r}) d\mathbf{r}}{\int_{\mathbb{T}^{3N_a}} p_{A_\star}(\zeta|\mathbf{r}) P_{A_\star}(\mathbf{r}) d\mathbf{r}}, \tag{14}$$

where the marginal probability of ζ cancels in Eq. (13) and appears as the denominator of Eq. (14) in the form $P_{A_\star}(\zeta) = \int_{\mathbb{T}^{3N_a}} p_{A_\star}(\zeta|\mathbf{r}) P_{A_\star}(\mathbf{r}) d\mathbf{r}$. Equation (14) corresponds to the expectation form of the Bayes formula.

If the distribution $P_{A_\star}(\mathbf{r})$ can be sampled, the above average can be well approximated owing to the ergodic theorem.

Given a sequence of N points $\{\mathbf{r}_s\}_{1 \leqslant s \leqslant N}$ sampled from the probability distribution $P_{A_\star}(\mathbf{r})$, the mean force is estimated as

$$A'(\zeta) = \frac{\sum_{s=1}^N \partial_\zeta U(\zeta, \mathbf{r}_s) p_{A_\star}(\zeta|\mathbf{r}_s)}{\sum_{s=1}^N p_{A_\star}(\zeta|\mathbf{r}_s)}, \tag{15}$$

where the conditional probabilities of ζ given the sampled points are directly calculated through numerical quadrature and the relation below:

$$p_{A_\star}(\zeta|\mathbf{r}) = \frac{\exp\left[-\beta U_{A_\star}(\zeta, \mathbf{r})\right]}{\int_0^1 \exp[-\beta U_{A_\star}(\tilde{\zeta}, \mathbf{r})] d\tilde{\zeta}}. \tag{16}$$

A simple way to sample the distribution $P_{A_\star}(\mathbf{r})$ consists in implementing an underdamped Langevin molecular dynamics:

$$d\mathbf{r}_t = \nabla_{\mathbf{r}}\{\beta^{-1} \ln[P_{A_\star}(\mathbf{r}_t)]\} dt + \sqrt{2\beta^{-1}} dW_t. \tag{17}$$

The first term of the right-hand side of Eq. (17) can be written as an effective force field:

$$\nabla_{\mathbf{r}}\{\beta^{-1} \ln[P_{A_\star}(\mathbf{r})]\} = -\int_0^1 \nabla_{\mathbf{r}} U(\zeta, \mathbf{r}) p_{A_\star}(\zeta|\mathbf{r}) d\zeta$$
$$= \mathbb{F}_{A_\star}(\mathbf{r}), \tag{18}$$

while the second term of the right-hand side of Eq. (17) represents the uncorrelated random forces with W_t denoting a $3N_a$-dimensional Wiener process. It satisfies the property $W_{t+u} - W_u \sim \mathcal{N}(\mathbf{0}, t\mathbf{I})$ where $\mathbf{I}$ is the identity matrix, i.e., $W_t - W_0 = \int_0^t dW_t$ is normally distributed with zero mean vector and $t\mathbf{I}$ variance matrix. In practice, we prevent the center of mass of the system from drifting with respect to the fixed reference lattice. To achieve this, we introduce a projection $\mathbf{P}$ that shifts the center of mass from any position to its initial position. This operator being symmetric and idempotent, we have $\mathbf{P} = \mathbf{P}\mathbf{P}^\top$. Consequently, the projected Langevin dynamics of the system reads

$$d\mathbf{r}_t = \mathbf{P}\mathbb{F}_{A_\star}(\mathbf{r}_t) dt + \sqrt{2\beta^{-1}} \mathbf{P} dW_t. \tag{19}$$

By definitions in Eqs. (2) and (5), we have $\forall z \in [0, 1]$,

$$\ln \frac{P_{A_\star}(\zeta = z)}{P_{A_\star}(\zeta = 0)} = \ln \frac{\int_{\mathbb{T}^{3N_a}} \exp\left[-\beta U_{A_\star}(z, \mathbf{r})\right] d\mathbf{r}}{\int_{\mathbb{T}^{3N_a}} \exp\left[-\beta U_{A_\star}(0, \mathbf{r})\right] d\mathbf{r}}$$
$$= \beta\{[A_\star(z) - A_\star(0)]$$
$$- [A(z) - A(0)]\}. \tag{20}$$

Therefore, once we obtain a uniform sampling of $P_{A_\star}(\zeta)$ over $\zeta \in [0, 1]$, we have $A_\star(z) - A_\star(0) = A(z) - A(0)$ which gives the difference in free energy from the difference of biasing potentials.

To implement the numerical algorithm, Eq. (19) is discretized. The $(n + 1)$th molecular dynamics move can be realized based on the first n steps with the following algorithm.

Step 1. $A'_n(\zeta)$ is computed as

$$A'_n(\zeta) = \frac{\sum_{s=1}^{n-1} \partial_\zeta U(\zeta, \mathbf{r}_s) p_{A_s}(\zeta|\mathbf{r}_s) w(s)}{\sum_{s=1}^{n-1} p_{A_s}(\zeta|\mathbf{r}_s) w(s)}, \tag{21}$$

where $\nabla_\zeta U(\zeta, \mathbf{r}_s)$, being exactly equal to $U(\mathbf{r}) - U_{\text{ref}}(\mathbf{r})$, is easy to evaluate and the weighting function $w(s)$, detailed in the following section, is introduced to accelerate the initial convergence.
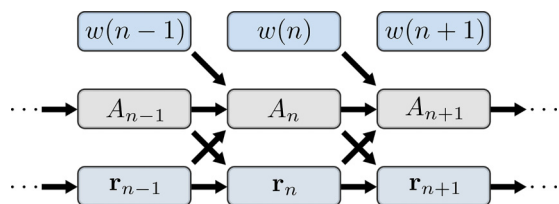
FIG. 2. Bayesian iterative flowchart of the present free energy sampling: The forward step integrates the whole history of the Langevin dynamics. The weight $w(n)$ is inserted at each integration step in order to accelerate the convergence of A_n and its form is a user choice as discussed in Sec. II D.

Step 2. The free energy $A_n(\zeta)$ for the step n is determined as

$$A_n(\zeta) = \int_0^\zeta A'_n(\tilde{\zeta}) d\tilde{\zeta} + A_n(0). \qquad (22)$$

Step 3. The corresponding conditional probability of ζ for a given $\mathbf{r}_n$ is calculated as

$$p_{A_n}(\zeta|\mathbf{r}_n) = \frac{\exp\left[-\beta U_{A_n}(\zeta, \mathbf{r}_n)\right]}{\int_0^1 \exp\left[-\beta U_{A_n}(\tilde{\zeta}, \mathbf{r}_n)\right] d\tilde{\zeta}}. \qquad (23)$$

Step 4. The effective force field is obtained by the equation

$$\mathbb{F}_{A_n}(\mathbf{r}_n) = -\int_0^1 \nabla_{\mathbf{r}} U(\zeta, \mathbf{r}_n) p_{A_n}(\zeta|\mathbf{r}_n) d\zeta. \qquad (24)$$

Step 5. Integration of the dynamic equation is carried out to obtain

$$\mathbf{r}_{n+1} = \mathbf{r}_n + \mathbf{P}\mathbb{F}_{A_n}(\mathbf{r}_n)\delta t + \sqrt{2\beta^{-1}\delta t} B_n, \qquad (25)$$

where $B_n \sim \mathcal{N}(\mathbf{0}, \mathbf{P})$ is a normal deviate with zero mean and $\mathbf{P}$ variance.

Once the new positions are determined, iteration continues until the desired accuracy of $A_n(\zeta)$ is achieved. Based on Eq. (20), we have $\lim_{n \to +\infty} \Delta A_n = \Delta A$. The iterative process is concisely illustrated by the flowchart in Fig. 2.

In practical applications, we analyze the sampling stability on the fly by monitoring the running estimate of the marginal probability at step n:

$$P_{A_n}(\zeta) = \frac{1}{n} \sum_{s=1}^n p_{A_s}(\zeta|\mathbf{r}_s), \qquad (26)$$

which is the mean value of the probability of ζ conditioned on the sampled states $\mathbf{r}_s$ during the Langevin dynamics and given the successive biasing potentials A_s, with $1 \leqslant s \leqslant n$. As a probability density, the integral of $P_{A_n}(\zeta)$ over $\zeta \in [0, 1]$ is 1. This distribution should be uniform in ζ in order to ensure that the difference in free energy of the target and reference systems becomes equal to the corresponding difference in the biasing potentials yielded by the adaptive Langevin dynamics, as expected from Eq. (20).

For assessing the relative efficiency of sampling using different reference systems and weighting functions, we also monitor the Kullback-Leibler (KL) divergence of $P_{A_n}(\zeta)$ from the uniform distribution:

$$D_{\mathrm{KL}}(P_{A_n}||\mathbf{1}_{[0,1]}) = \int_0^1 P_{A_n}(\zeta) \ln \frac{P_{A_n}(\zeta)}{\mathbf{1}_{[0,1]}(\zeta)} d\zeta. \qquad (27)$$

This statistical pseudonorm measures how close the probability distribution $P_{A_n}(\zeta)$ is to the uniform distribution $\mathbf{1}_{[0,1]}(\zeta)$. It is zero for identical distributions and infinite for nonoverlapping distributions. The closer to zero the KL divergence is, the better the adaptive sampling procedure has converged. The reason is that the biasing potential integrated from a well-converged biasing force yields a reliable estimate of the free energy $A(\zeta)$. The recorded marginal probability of ζ, $P_{A_n}(\zeta)$ from Eq. (26), should thus converge towards $P_A(\zeta)$ that corresponds to the uniform probability distribution over [0,1] range, which is $\mathbf{1}_{[0,1]}(\zeta)$.

C. Choice of reference system

Hoover and Ree's single-occupancy cell (SOC) method [57,58] is one of the first methods proposed to obtain a reference system in the form of an artificial solid. According to the SOC method, each of the N_a atoms in the system is confined in its own cell of volume V/N_a at all densities to ensure that no melting occurs and the solid-phase thermodynamic properties of this artificial solid hold true. Though unphysical, this method was successfully applied to the calculation of the free energy of hard spheres [57] using computer simulations. Hoover *et al.* [59,60] also suggested an alternative method which involved a two-step calculation [7]. In the first step, the given solid is approximated as a harmonic crystal by cooling it to a sufficiently low temperature and then the free energy of this solid can be analytically calculated using lattice dynamics. The second step involves using the result from the first step as a reference to calculate the free energy at a given higher temperature. However, both methods have some drawbacks. For instance, numerical integration for the SOC method is complicated for unstable solids where phase transitions may occur; cooling used to obtain a harmonic crystal may not be reversible, etc.

In order to improve the performance of the method, other useful references have been proposed, such as Einstein crystal [61,62], harmonic solid [63,64], Morse potential [4], Lennard-Jones system [9], inverse power potential [8,9], EAM [8,65], MTP [13], and linear combination of the potentials above [8].

In this paper only reference systems with analytically known free energy are considered. We test the use of Einstein and harmonic approximations and further optimize the harmonic reference. We demonstrate that such simple references are sufficient to provide accurate and efficient calculations with the BABF approach.

1. Einstein approximation

The Einstein crystal has been used extensively as a reference system in free energy calculations since the works of Broughton and Gilmer [66] and Frenkel and Ladd [61], due to the simplicity of its formalism and implementation. In Einstein approximation (EA), it is assumed that the atoms oscillate independently about their mechanical equilibrium positions denoted by $\mathbf{r}_0 \in \mathbb{T}^{3N_a}$, i.e., the lattice vibrations are represented by N_a three-dimensional classical distinguishable oscillators, yielding $3N_a$ oscillators with an average frequency ω_i for $i = 1, \ldots, 3N_a$ and atomic mass m_i. The Hamiltonian

of the Einstein system has the following potential energy:

$$U(\mathbf{r}) = U(\mathbf{r}_0) + U_{\mathrm{EA}}(\mathbf{r}, \mathbf{r}_0),$$

$$U_{\mathrm{EA}}(\mathbf{r}, \mathbf{r}_0) = \frac{1}{2} \sum_{i=1}^{3N_a} m_i \omega_i^2 (r_i - r_{i,0})^2. \tag{28}$$

For the special case where all atoms have the same mass $m_i = m$ and vibrate at the same frequency $\omega_i = \omega$, the free energy can be written as

$$F_{\mathrm{EA}} = 3N_a \beta^{-1} \ln \beta \hbar \omega. \tag{29}$$

As previously emphasized, our aim is to construct a reversible path from the noninteracting Einstein crystal to the crystal of interest. This implies that the lattice of the reference system at mechanical equilibrium should coincide with that of the target crystal. This condition can be ensured by harmonically coupling (via springs) the center of mass of the Einstein crystal to that of the crystal of interest. According to Ryckaert and Ciccotti [67], Eq. (29), for a constrained system, can be written as

$$F_{\mathrm{EA, c}} = (3N_a - 3) \beta^{-1} \ln \beta \hbar \omega. \tag{30}$$

The main drawback of EA is that the Einstein frequency needs to be calibrated very carefully, because even a small variation in frequency can produce a large difference in the free energy of the reference and target crystals and result in computational overhead. Using Eq. (30), this calibration can be performed through the harmonic free energy calculation of a small system:

$$\omega(\beta) = \frac{1}{\beta \hbar} \exp \left[\frac{\beta F^{\mathrm{bulk}}(\beta)}{3N_a - 3} \right], \tag{31}$$

taking into account the temperature dependence of ω. For instance, the full anharmonic free energy $F^{\mathrm{bulk}}(\beta)$ can be quickly estimated in a short simulation at inverse temperature β using a system with a small number of atoms (in the case of bcc lattice, a $2 \times 2 \times 2$ simulation cell with 16 atoms may be sufficient) and then, through the estimated value of $\omega(\beta)$, scaled to a larger system.

2. Harmonic approximation

Alternatively, the reference system can be built upon the harmonic approximation (HA), which involves a second-order Taylor expansion of the potential energy around the mechanical equilibrium:

$$U(\mathbf{r}) = U(\mathbf{r}_0) + U_{\mathrm{HA}}(\mathbf{r}, \mathbf{r}_0),$$

$$U_{\mathrm{HA}}(\mathbf{r}, \mathbf{r}_0) = \frac{1}{2} \sum_{i,j=1}^{3N_a} K_{ij} (r_i - r_{i,0})(r_j - r_{j,0}) \tag{32}$$

where the Hessian matrix of the potential energy at the minimum defines the force constants $K_{ij} = \frac{\partial^2 U(\mathbf{r})}{\partial r_i \partial r_j}|_{\mathbf{r}=\mathbf{r}_0}$. Moreover, the force field deriving from the HA potential has a computational complexity of $\mathcal{O}(N_a^2)$, as can be inferred from the double summation appearing in Eq. (32). However, the quadratic complexity can be turned linear since the atomic interactions are ignorable beyond some cutoff distance R_{cut}

and therefore the force constants K_{ij} are zero above $2R_{\mathrm{cut}}$ interatomic distance, i.e., the sum in Eq. (32) can be reorganized as

$$U_{\mathrm{HA}}(\mathbf{r}, \mathbf{r}_0) = \frac{1}{2} \sum_{i=1}^{3N_a} \sum_{j \in v(i)} K_{ij} (r_i - r_{i,0})(r_j - r_{j,0}), \tag{33}$$

for which $v(i)$ is the collection of neighbor atoms of the ith atom within $2R_{\mathrm{cut}}$ distance. These summations have $\mathcal{O}(N_a n)$ computational complexity, where n is the average number of neighbor atoms within $v(i)$ (in general for large systems $n \ll N_a$).

In the present case the HA development is performed around a minimum $\mathbf{r}_0$ of the potential energy, which means that HA contribution in Eq. (32) is a positive semidefinite quadratic form and so matrix $\mathbf{K} = [K_{ij}]$ is symmetric and non-negative. Defining the reference system based on an approximation accounting for all vibration frequencies of the physical system provides an important advantage: The degree of overlap between the reference and target distribution is expected to be high. Besides, the free energy difference between the target and reference systems should be relatively small, at least at reasonable temperatures lower than one third of the melting point.

The partition function, from which the harmonic free energy is deduced, is obtained by writing the Hamiltonian in normal coordinates and solving the decoupled equations of motion. The normal modes correspond to the eigenvectors of the dynamical matrix $D_{ij} = K_{ij} / \sqrt{m_i m_j}$. Note that the dynamical matrix has only real values in the present paper because we treat only the Γ-HA modes, i.e., those in the center of the Brillouin zone of the crystal.

Being also symmetric non-negative, the matrix $\mathbf{D}$ is diagonalizable with real non-negative eigenvalues whose square roots define the frequencies of the normal modes. We sort the frequencies in descending order by convention: $\omega_1 \geqslant \omega_2 \geqslant \cdots \geqslant \omega_{3N_a-3} > 0$. Here, frequencies are strictly positive except the three last ones that are exactly zero due to the periodic boundary conditions that are applied to our atomistic simulations. The null-space normal modes characterize the three translation symmetries of the overall system in the three-dimensional physical space.

In the limit of high temperature, the phonons (normal modes) behave as independent and Boltzmann-distributed classical oscillators, so the free energy becomes

$$F_{\mathrm{HA}} = \beta^{-1} \sum_{i=1}^{3N_a-3} \ln (\beta \hbar \omega_i). \tag{34}$$

It should be noted that employing directly the HA potential energy [Eq. (32)] as the reference system may lead to unstable and nonconverging dynamics in some cases, especially at saddle points separating local energy minima, for which negative eigenvalues of $\mathbf{D}$ exist.

The sampling instability in a physically stable state, like bulk tungsten, stems from the fact that the three translation eigenvalues are not exactly zero as they should be. These lowest eigenvalues correspond to the overall displacement of the system along three directions through the periodic boundaries.
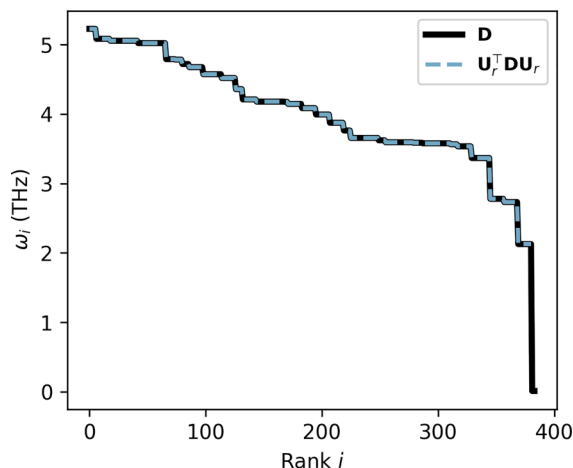
FIG. 3. Phonon frequencies ω_i derived from the eigenvalues ω_i^2 of the dynamical matrix $\mathbf{D} \in \mathbb{R}^{384 \times 384}$ of 128 atoms in pure bcc W at equilibrium and the filtered matrix $\mathbf{U}_r^\top \mathbf{D} \mathbf{U}_r$, where $r = 381 = 3 \times 128 - 3$ and $\mathbf{U}_r \in \mathbb{R}^{384 \times 381}$ is the matrix of the first r left singular vectors of $\mathbf{D}$.

In exact arithmetic, the null space that reflects the translation symmetries does not affect the dynamics because the center of mass is shifted to its initial position at each step, which means that the displacement vector $\mathbf{r} - \mathbf{r}_0$ remains orthogonal to the null space. However, in finite-precision arithmetic, rounding errors in the evaluated eigenvectors result in a nonzero projection of the displacement vector onto the computed null space. As soon as a translation eigenvalue becomes slightly negative, it generates forces that favor the atomic motion away from the unstable equilibrium position. Hence, excessive atomic displacements may occur whenever the dynamics is dominated by the harmonic potential.

To address this problem, we develop and test another numerical scheme, in which we force the translation eigenvalues of the dynamical matrix to be strictly equal to zero so that the gradient of the harmonic potential in Eq. (32) is null along translation symmetries and the dynamics is always orthogonal to this null space. To achieve this goal, a numerical filter based on SVD is proposed. The SVD decomposition of the real dynamical matrix $\mathbf{D} = [D_{ij}] \in \mathbb{R}^{3N_a \times 3N_a}$ is given by

$$
\begin{aligned}
\mathbf{D} &= \mathbf{U}\boldsymbol{\Sigma}\mathbf{V}^\top, \\
\mathbf{U} &= U_1 \ldots U_{3N_a}
\end{aligned}
\tag{35}
$$

with $U_i \in \mathbb{R}^{3N_a \times 1}$ are the $3N_a$ left singular vectors whereas $\boldsymbol{\Sigma}$ and $\mathbf{V}$ contain the singular values and the right singular vectors. We filter the spurious modes associated with the three lowest eigenvalues by projecting the constant matrix $\mathbf{D}$ into the subspace spanned by the first $3N_a - 3$ right singular vectors $\mathbf{U}_r = (U_1 \ldots U_r) \in \mathbb{R}^{3N_a \times r}$ where $r = 3N_a - 3$. The projector ensuring this transformation is $\mathbf{U}_r \mathbf{U}_r^\top$. In this way, $\mathbf{K} = [D_{ij}\sqrt{m_i m_j}]$ in Eq. (32) is replaced by $\mathbf{K}^{\mathrm{SVD}} = [D_{ij}^{\mathrm{SVD}}\sqrt{m_i m_j}]$ where $\mathbf{D}^{\mathrm{SVD}} = \mathbf{U}_r \mathbf{U}_r^\top \mathbf{D} \mathbf{U}_r \mathbf{U}_r^\top$ (see Fig. 3). The bottleneck here is the SVD decomposition whose computational complexity is cubic but which, fortunately, should be made only once, as a separate calculation before the sampling procedure begins. Note that evaluating the filtered potential energy has the same scalability as that for evaluating the

nonfiltered potential energy. The computational complexity is linear when the null-space components of the position vector are filtered out prior to calling the neighboring list defined in Eq. (33).

For the perfect bulk tungsten where no negative eigenvalues exist apart from the three translation eigenvalues, the applications of the SVD filter and the $\mathbf{P}$ projector in Eq. (19) are equivalent. However, SVD filtering is more general. Using the SVD-filtered potential is expected to improve the stability of mean force sampling by preventing the reference dynamics from diverging. It should therefore be useful in sampling unstable transition states.

3. Comparison between Einstein and harmonic approximations

Here we compare the convergence of the biasing force towards the mean force using the BABF method for which the reference system is based on the Einstein or harmonic approximations. The target physical system consists of W atoms described by an EAM potential [68]. To assess finite size effects, we first performed two preliminary simulations in systems containing 128 and 1024 atoms at 3400 K. The variation of the lattice constant in BABF calculations with those systems is of the order of 10^{-4} Å. The associated difference in bulk modulus is 1 GPa (the relative error is 0.37%). Considering this error to be acceptable, we conclude that the small system size of 128 atoms does not limit the accuracy of the BABF calculations. Therefore, all simulations in the following part of the paper are carried out with 128 atoms, unless otherwise specified.

The behavior of the BABF method using the standard HA reference (denoted by HA) and the SVD-filtered harmonic reference (denoted by HA-SVD) is first briefly discussed. As explained in Sec. II C 2, using the projection $\mathbf{P}$ that shifts the center of mass from any position to its initial position at each dynamic step is equivalent to filtering the HA reference via SVD decomposition in this case (perfect bulk crystal). Hence, either of the two methods is able to stabilize the dynamics. This equivalence is demonstrated by the overlapping curves of recorded marginal probability $P_{A_n}(\zeta)$ at $n = 2000$ for HA and HA-SVD references displayed in Fig. 4(a). Since the SVD filter is a more general approach, the standard HA reference will not be investigated anymore in the following sections. We rather focus on the SVD-filtered harmonic reference, denoted by HA-SVD, and thus compare EA and HA-SVD references implemented in BABF simulations. The recorded marginal probabilities $P_{A_n}(\zeta)$ at $n = 2000$ for the two references are also displayed in Fig. 4(a), from which we observe a more uniform sampling when HA-SVD, rather than EA, is used as reference. We further assess the sampling performance by computing the KL divergence of $P_{A_n}(\zeta)$ from the uniform distribution [see Eq. (27)].

As illustrated in Fig. 4(b) where the KL divergence is plotted as a function of n, the convergence level achieved after 80 000 Langevin steps using the Einstein reference necessitates three times more steps than when using the SVD-filtered harmonic reference instead. This trend is explained by the fact that the harmonic solid is more supple than the Einstein solid, as the harmonic Hamiltonian includes information from all possible pairwise interactions, while the Einstein formal-
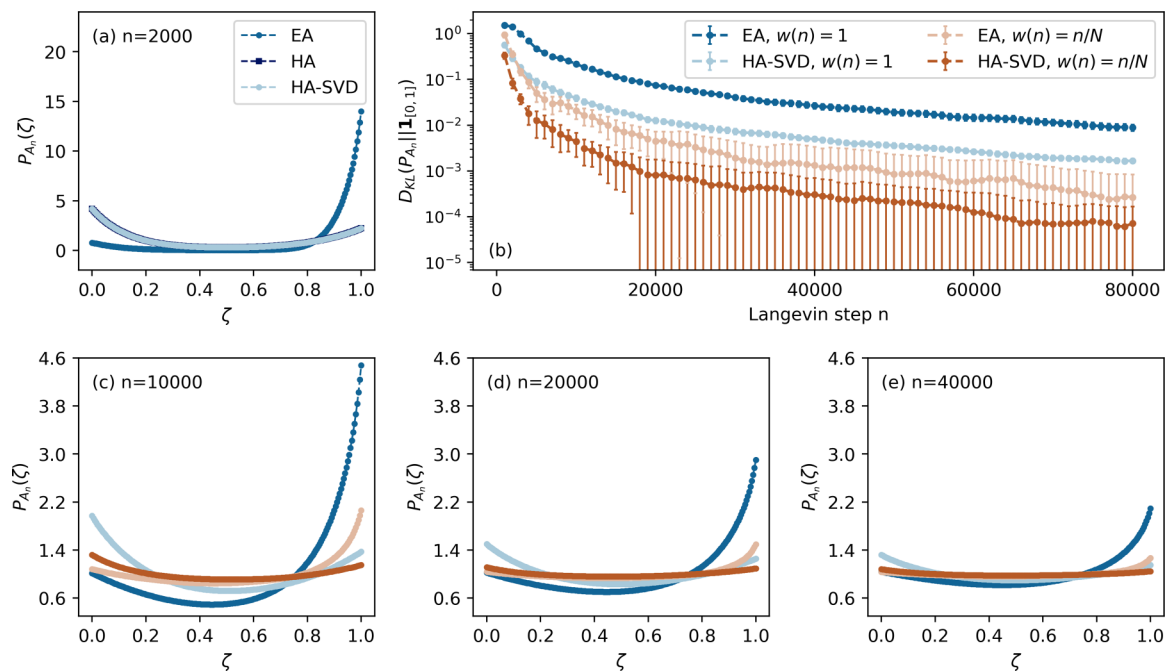
FIG. 4. (a) Distribution of the estimated marginal probability $P_{A_n}(\zeta)$ at Langevin step $n = 2\,000$ of BABF calculations using references with Einstein approximation (EA), standard harmonic approximation (HA), and SVD-filtered harmonic approximation (HA-SVD). (b) Variation of KL divergence for the BABF calculations with EA reference and HA-SVD reference. (c–e) Distribution of $P_{A_n}(\zeta)$ at Langevin step (c) $n = 10\,000$, (d) $n = 20\,000$, and (e) $n = 40\,000$ of the calculations shown in (b). No weighting function [$w(n) = 1$] is applied in (a), while two cases of weighting function [$w(n) = 1$ and n/N] are considered in (b)–(e), where N is the total number of Langevin steps. Legends for (c) and (d) are the same as that in (b). All the calculations in this figure are performed in a bcc W system of 128 atoms at 3400 K using the WEAM4 potential [68].

ism considers a set of independent but identical harmonic oscillators.

Additional profiles of the probability distributions $P_{A_n}(\zeta)$ are shown in Figs. 4(c)–4(e) at increasing n values and using two types of weighting functions $w(n)$ in Eq. (21). The linear weighting function $w(n) = n/N$ where N denotes the total number of steps is implemented in addition to the constant function $w(n) = 1$ used previously. For both weighting functions, the distribution $P_{A_n}(\zeta)$ flattens faster with the filtered harmonic reference than with the Einstein reference, which indicates a better sampling performance of the former. In contrast, the use of the latter results in excessively high probability on both sides, especially around $\zeta = 1$. We further observe from Figs. 4(b)–4(e) that convergence is significantly improved by the use of the linear weighting function. We next investigate the impact of the weighting function on the convergence behavior of the BABF method with HA-SVD reference.

D. Choice of weighting function

As emphasized in Fig. 4, one should notice that the first several iterations of the BABF method give relatively biased sampling of ζ. Hence, a weighting function reevaluated at each step is set in Eq. (21) to reduce the contribution of the configurations initially sampled and then improve the sampling efficiency. In Fig. 4, results of the simplest linear weighting function $w(n) = n/N$ for $n = 1, \ldots, N$ are compared with the case without weighting function [$w(n) = 1$]. Application of weighting results in significant

improvement of sampling efficiency. To reach the convergence level $D_{\mathrm{KL}}(P_{A_n} || \mathbf{1}_{[0,1]}) < 10^{-3}$ with harmonic reference, 20 000 steps of Langevin dynamics are sufficient through linearly weighting the sampling, while 80 000 steps are still not enough without the use of the weighting function. Consequently, it is of great interest to figure out the effects of the weighting function.

Several weighting functions varying from 0 to 1 are tested in order to measure the impact of the functional form. Figure 5 illustrates the results of employing the various weighting functions that have been selected. The different shapes of these functions are illustrated in Fig. 5(a). To evaluate the importance of the first n samples, we display the following characteristic function $w(n)/\sum_{s=1}^{n} w(s)$ in Fig. 5(b), while the corresponding KL divergence is shown in Fig. 5(c). The weighting function with larger value of $w(n)/\sum_{s=1}^{n} w(s)$ at $n \ll N$ leads to faster convergence [Figs. 5(b) and 5(c)] since it lowers the contribution of the initial sampling. From this analysis it can be concluded that an appropriate choice of weighting function, such as $w(n) = [\sin(\frac{n\pi}{2N} - \frac{\pi}{2}) + 1](\frac{n}{N})^2$, can further improve the sampling significantly in terms of convergence speed: It requires only 6000 steps to attain $D_{\mathrm{KL}}(P_{A_n} || \mathbf{1}_{[0,1]}) < 10^{-3}$, which is three times faster than using the linear weighting function.

E. Comparison of BABF method and molecular dynamics on bulk modulus calculation

In this subsection we compare the performance of the present BABF method with classical MD simulations. The
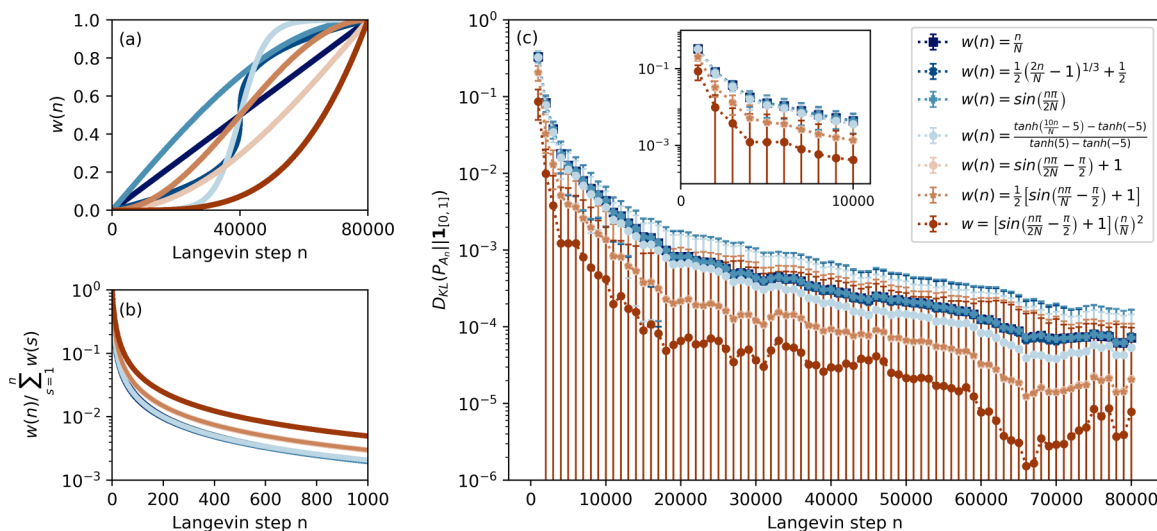
FIG. 5. (a) Shape of different weighting functions. (b) The value of $w(n)/\sum_{s=1}^{n} w(s)$, which determines the convergence speed. (c) Variation of KL divergence for different weighting functions. Legends for (a) and (b) are the same as that in (c). All the results in this figure are obtained by BABF calculations with HA-SVD reference based on the same bcc W system and the same EAM potential as in Fig. 4.

direct comparison on free energy calculations is out of scope. It is well known that direct MD simulations are unable to estimate the free energy of the system. Here, we instead perform an indirect comparison on the second derivative of the free energy with respect to the volume of the system, i.e., the isothermal bulk modulus B^T.

The previous BABF method with both EA and HA-SVD references is used to compute the free energy at 20 temperatures ranging from 10 to 3800 K. At each temperature, a series of deformed systems is considered, allowing one to extract the bulk modulus from the second derivative of the free energy versus volume curve. Details of the procedure are illustrated in Fig. 6.

The bulk moduli from MD-based simulations are obtained by measuring the change in average stress tensor when the cell volume undergoes a finite deformation [69] with the ELASTIC_T package available in LAMMPS [70]. The high temperatures 3000, 3400, 3600, and 3800 K, for which the thermal fluctuations are large, have been selected.

The bulk modulus computations using both methods are made within a bcc W system modeled with WEAM4 potential [68]. A system containing 128 atoms is used in BABF calculations, while 16 000 atoms are needed in MD simulations to avoid excessive fluctuations.

The relative error is recorded in BABF and MD simulations for the system at 3400 K and plotted in Fig. 7(a). One notices that the BABF calculation with EA reference exhibits a significantly larger initial relative error than that obtained with HA-SVD reference. BABF calculations with both references converge quickly. Specifically, the relative error of BABF calculation decreases to less than 1% from step 8000 with EA reference and from step 2000 using HA-SVD reference. In contrast, MD simulation starts with a slight error but always suffers severe fluctuations so that a large number of MD steps are required to obtain a reliable time average. Thus, the much smaller number of integration steps, combined with the small system size in the BABF approach, results in a 100-fold increase in computational efficiency.

The results of BABF with EA and HA-SVD references are consistent with those obtained from MD simulations [Fig. 7(b)]. The obtained agreement validates the further application of the optimized BABF method to the calculations of elastic properties and thermal expansion. From the cost analysis, we conclude that the present method is fast and robust for estimating the free energy in crystalline solids and
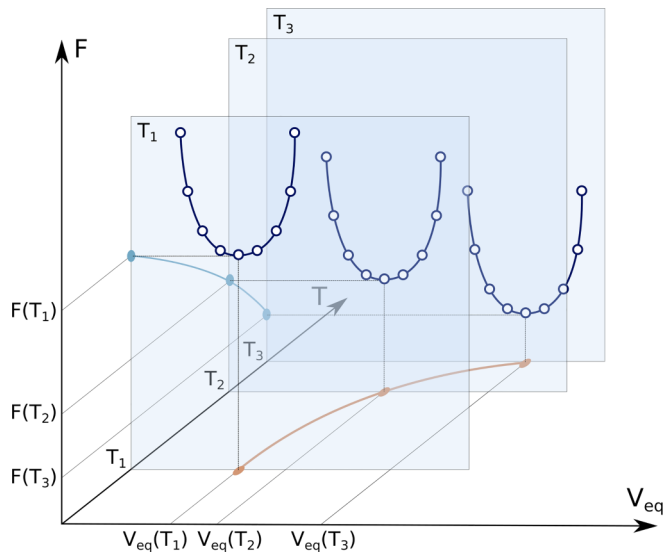

FIG. 6. Illustration of thermodynamic properties calculation with the BABF method, where V_{eq} and F denote the equilibrium volume and the Helmholtz free energy, respectively. At temperature T, we compute the free energy for a series of systems with different volumes as presented by the dark blue curves. The value of the lattice constant corresponding to V_{eq}, i.e., the free energy minimum, is the lattice constant at this temperature, from which the volumetric thermal expansion can be obtained (dark orange curve). Bulk modulus is proportional to the second derivative of the free energy with respect to the volumetric strain. Temperature dependence of the free energy minimum (light blue curve) allows the entropy evaluation.
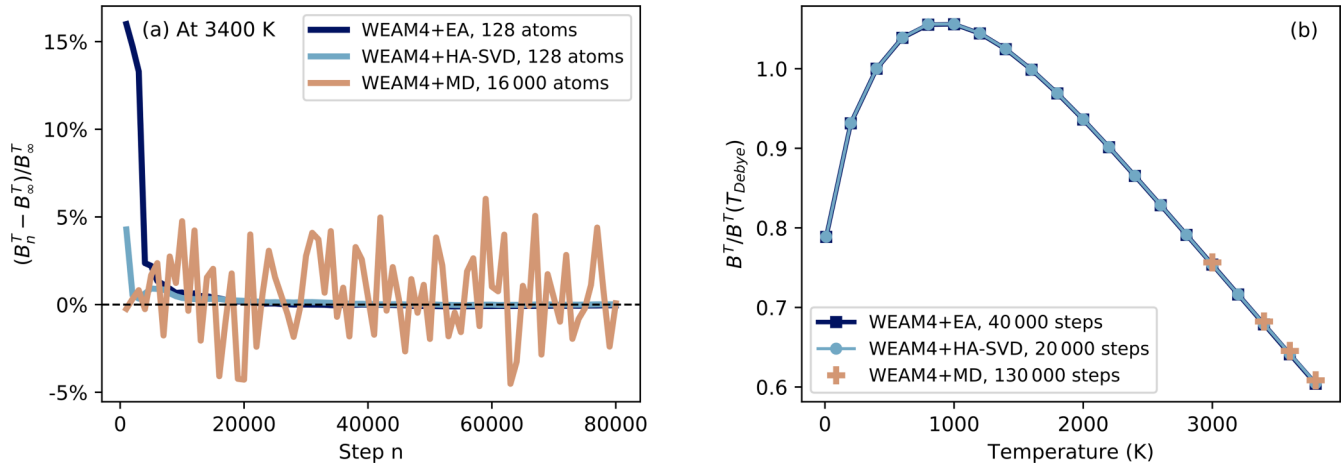
FIG. 7. Comparison of BABF method and MD simulation. (a) Runtime relative error $(B_n^T - B_\infty^T)/B_\infty^T$ at 3400 K with B_∞^T the fully converged value. (b) Rescaled bulk modulus as a function of temperature. We take the ratio of the bulk modulus at temperature T to its value at the Debye temperature T_{Debye}, equal to 400 K for W [71]. The dark blue and light blue lines are computed with BABF method without weighting function using EA and HA-SVD references, respectively. The dark orange line is obtained from MD simulations. The number of atoms in the bcc W system and the number of iteration steps to achieve the convergence for each method are indicated in the legends. All the curves are obtained with the WEAM4 potential [68].

can be applied to sample not only fast standard force fields but also numerically heavy machine learning potentials [46,72–74].

III. APPLICATION TO BCC TUNGSTEN

Tungsten is a potential first-wall material near the divertor area in a fusion reactor due to its high melting point, high temperature strength, and high thermal conductivity [43,44]. Based on the bulk modulus calculations of W, the performance of the optimized BABF method from Sec. II is validated over a wide range of temperature. Furthermore, fast calibration and optimization of ML interatomic potentials are carried out with the application of the above method. Throughout Sec. III all the BABF simulations are performed using the HA-SVD reference unless otherwise stated. To construct the model of temperature-dependent elastic constants for bcc W, we conduct the BABF-HA-SVD calculations using different interatomic potentials in a wide range of temperature (10 to 3800 K), and compare the results with the experimental values, available in the range between 4.2 and 2 073.15 K [51,52]. Isothermal elastic properties from experiments can be derived from the following relations:

$$
\begin{aligned}
C_{11}^T &= C_{11}^S - B^S + B^T, \\
B^T &= \frac{C_P B^S}{C_P + T V \alpha^2 B^S}, \\
C'^T &= C'^S, \quad C_{44}^T = C_{44}^S,
\end{aligned}
\tag{36}
$$

where $C' = \frac{1}{2}(C_{11} - C_{12})$; C_{11}, C_{12}, and C_{44} are the elastic constants in Voigt notations characterizing cubic crystals; C_P and α denote, respectively, the experimental isobaric heat capacity and the volumetric thermal expansion [51–53,75,76]. The superscript T represents the isothermal quantities, while the superscript S indicates the adiabatic results, which can be obtained from the experiments. Here, for each temperature,

the elastic properties are rescaled by the corresponding values at the Debye temperature T_{Debye}, equal to 400 K for W [71].

The adiabatic elastic constants of W were successively measured by pure continuous wave techniques (from 77 to 500 K [50]), pulse-echo techniques (from 4.2 to 300 K [51] and from 297.15 to 2073.15 K [52]), and sampled continuous-wave techniques (from 4.2 to 77 K [49]). To develop a high-temperature model which cannot be experimentally achieved, an empirical $cB\Omega$ model [77] of self-diffusion was applied to determine the bulk modulus of W [78]. With this model, Wang and Reeber evaluated the tungsten bulk modulus from self-diffusion, thermal expansion, and specific heat data over a wide range of temperatures (300–3600 K) [53]. Besides, Gustafson provided a polynomial expression of isothermal bulk modulus for W through evaluating the available experimental data [79], based on which Saxena and Zhang gave an estimation up to 3700 K [54].

A. Performance of EAM potentials

First, we perform the calculations using the present BABF-HA-SVD method and five different traditional EAM potentials: WDD by Derlet *et al.* [80], WEAM2 and WEAM4 by Marinica *et al.* [68] (denoted as EAM2 and EAM4 in Ref. [68]), WJW by Juslin and Wirth [81]), as well as WMB by Mason *et al.* [82], commonly used for atomic-scale modeling of bcc W. As reported in Fig. 8, none of the five EAM potentials can correctly reproduce the experimental curves. The curves of WDD and WMB strongly deviate from that of the experiments. WEAM2 and WEAM4 provide an opposite trend up to 800 K compared to the experiments: For C_{11}^T, C_{12}^T, and C_{44}^T, the computed values augment while the measured values decrease with increasing temperature. The WJW potential can describe the decreasing tendency of elastic constants. Nevertheless, the slope is too large, and abnormal fluctuation occurs at high temperature due to the potential instability. There are several reasons why these potentials can-
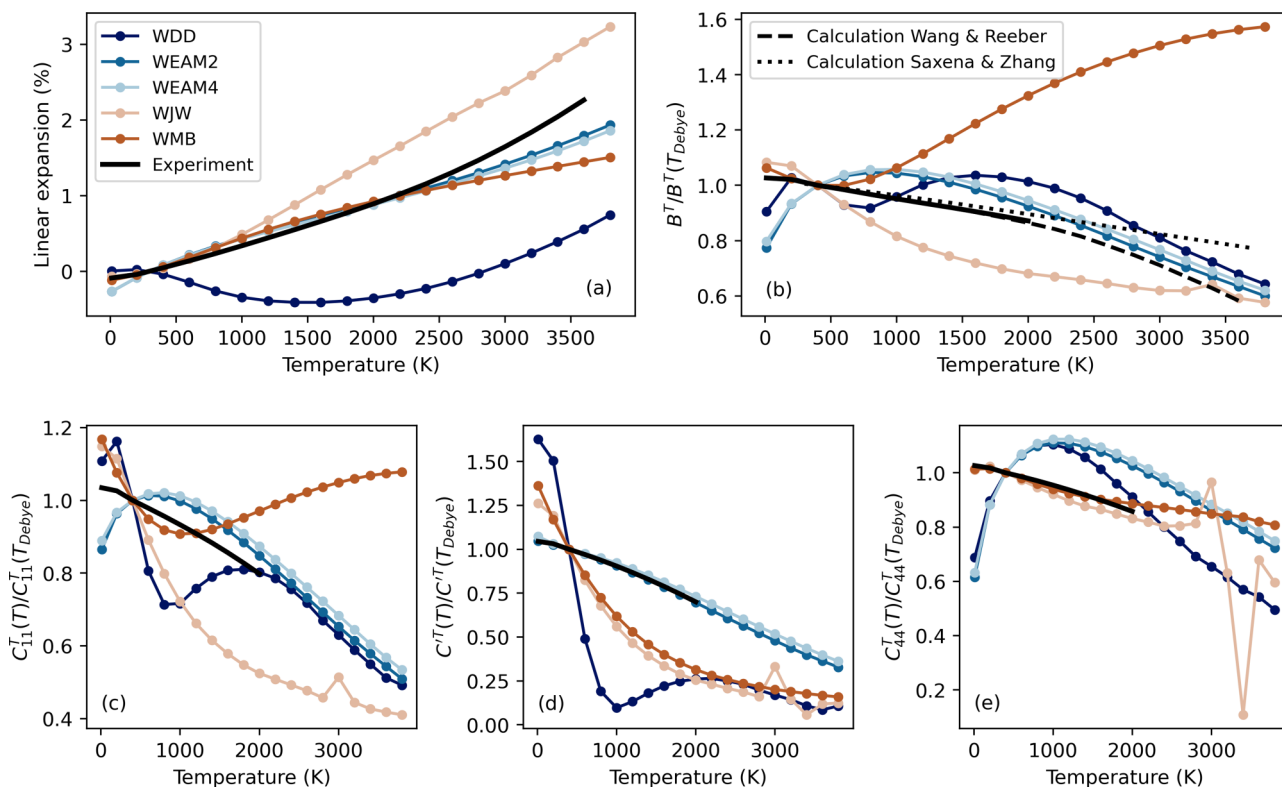
FIG. 8. (a) Linear thermal expansion, (b) rescaled bulk modulus, and (c–e) rescaled elastic constants of bcc W, from 0 K to the melting point, computed employing BABF-HA-SVD method and five different traditional EAM potentials: WDD [80], WEAM2 [68], WEAM4 [68], WJW [81], and WMB [82]. We take the ratio of the elastic properties at temperature T to its value at the Debye temperature $T_{\mathrm{Debye}} = 400$ K [71]. In all panels, the circles denote the results of BABF-HA-SVD calculations with respective force fields whereas the black lines and dash-dotted black lines are experimental [52] and calculated values [53,54], respectively. All the subplots share the legend provided in (a) and (b).

not correctly reproduce the temperature dependence of elastic constants in W.

(i) First the formalism is too basic to take into account the fact that W is a metal for which the Fermi level lays into a pseudogap [68,83]. This fact enhances the angular characters of the bonds, which cannot be reproduced by the radial many-body EAM force fields.

(ii) For all these potentials the database of fitting is very poor, without too much data beyond 0 K (except WEAM2 and WEAM4 for which a few W liquid configurations are included).

The relatively simple physical model of EAM formalism as well as in the fitting information does not allow one to accurately predict the high-temperature properties of W such as the evolution of bulk modulus with temperature [Fig. 8(b)]. Therefore, in the next section, we will turn to the class of ML potentials, which provide a remarkable improvement of accuracy compared with the empirical potentials [45–47] especially for W [48,84,85].

B. Prediction of elastic properties based on existing ML potentials

As previously stated, the traditional EAM force fields fail to reproduce thermoelasticity of bcc W. Employing the fast and robust BABF-HA-SVD method developed in the present paper, we will run through the numerically heavy but accurate

ML force fields. During the past several years, various types of ML interatomic potentials have been developed for W, which are most commonly based on the kernel methods, including the Gaussian approximation potential (GAP) [84,85], linear potential [48,86], and quadratic noise potential [48]. Moreover, the framework of deep learning neural networks is also used to construct the potential model for W [87].

In this section, we perform the BABF-HA-SVD calculations of elastic properties and thermal expansion in bcc W using different types of ML potentials and compare our results with the experimental values [51,52]. First, we investigate the existing recent ML potentials for W, which are constructed with linear formalism (LML) and quadratic noise formalism (QNML) [48]. These potentials are designed for the simulation of point and extended defects and the underlying database contains some finite-temperature W systems such as bulk and liquid state. The numerical cost (CPU time) per Langevin step of these ML potentials is a few tens times higher up to four orders of magnitude higher than with the EAM potentials but is much lower than the same accurate DFT calculation. The linear expansion and elastic properties given by both ML potentials (Fig. 9) are in much better agreement with the experimental results compared to those from the EAM potentials (Fig. 8). However, the rescaled bulk modulus calculated with QNML starts deviating from the experimental curve around 1000 K [Figs. 9(b)]. In addition, the calculations of the elastic constants, e.g., C_{44} in Fig. 9(e), reveal the limitations of the
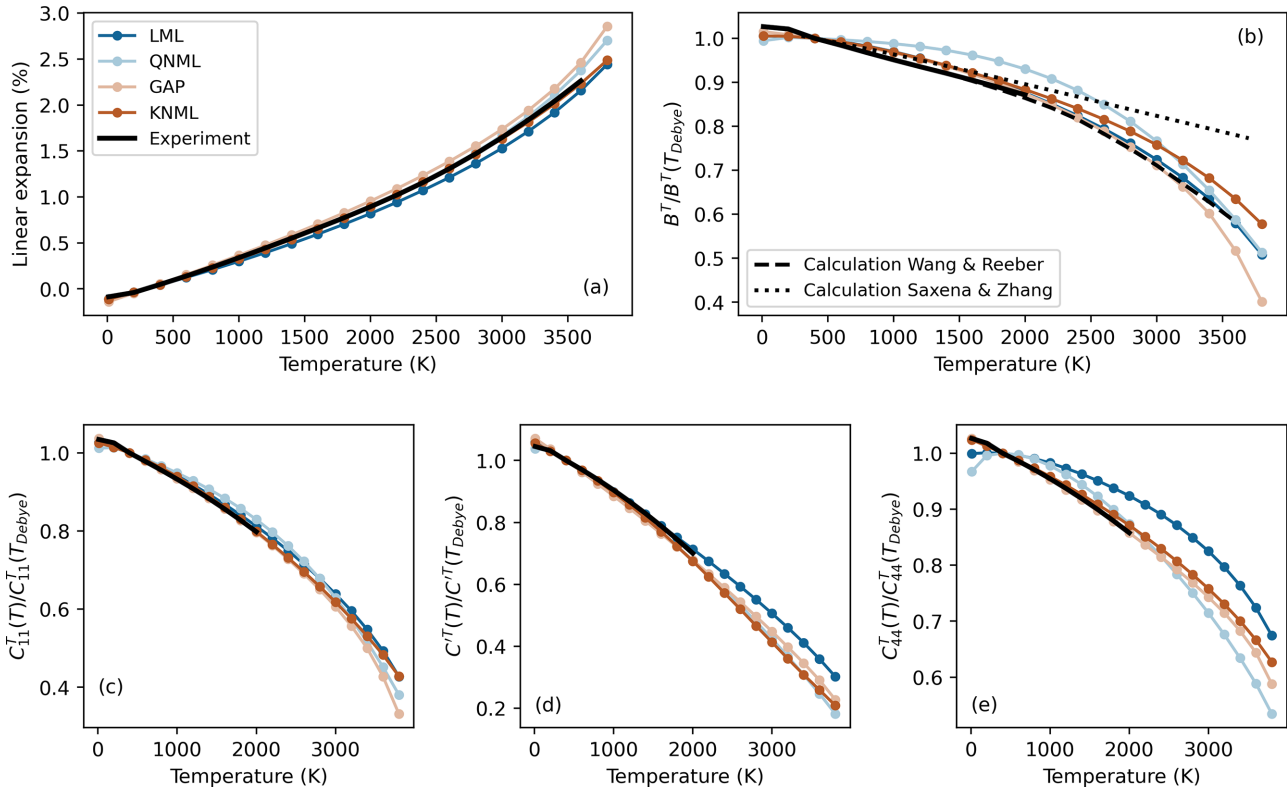
FIG. 9. The same elastic properties of bcc W as in Fig. 8, evaluated using ML potentials with different formalism: LML [48], QNML [48], GAP [84], and KNML. In all panels, the circles denote the results of BABF-HA-SVD calculations with respective force fields whereas the black lines and dash-dotted black lines are experimental [52] and calculated values [53,54], respectively. All the subplots share the legends provided in (a) and (b).

two ML potentials for the calculations of high-temperature elasticity.

Therefore, the widely used model GAP [84] for bcc W is considered. High efficacy and robustness of the present BABF-HA-SVD approach make it feasible to employ this computationally heavy force field, of which the numerical cost per Langevin step is about 15 times higher than that of the LML and QNML potentials. As shown in Fig. 9, the previously mentioned deficiencies of LML and QNML are dealt with using the GAP. Nevertheless, the linear expansion obtained with GAP deviates from the experimental curve at high temperatures. This can be explained by the lack of configurations above 1000 K in the database of GAP. In the next section we present the strategy to improve the accuracy of these high-temperature properties prediction based on BABF-HA-SVD in conjunction with ML force fields.

C. BABF-based strategy for ML potential improvement

The learning capacity of machine learning force fields can be increased by changing the formalism while the transferability can be optimized by increasing the size and the morphologies of the atomic environments in the database. First, we note that no configuration above 1000 K exists in the training database of the GAP force field, while in that of LML and QNML, only the configurations at 300, 1000, and 3000 K exist. However, the results of the GAP formalism seem to be very good until 2000 K compared with the experiment and

more reliable than the numerically efficient but lower capacity models yielding the LML and QNML potentials. Therefore, we propose to enlarge the database by collecting information from a wider range of temperatures and simultaneously increasing the learning capacity of the ML model. Here, the descriptors used previously within linear and quadratic noise regression to construct the LML and QNML force fields are similarly employed in the higher capacity kernel-based models. We also use the Machine Learning Dynamics (MILADY) package [48,86] to construct the associated force field.

To complete the database, MD simulation in the *NPT* ensemble is carried out using the LAMMPS-MILADY module [70]. The simulation system contains 128 atoms, and the temperature varies linearly from 100 to 5000 K in 245 000 steps. From the MD simulation, 38 configurations are randomly selected and then recalculated with DFT using VASP 6.2.0 [88] and the projector augmented wave pseudopotential for W that accounts for 14 valence electrons $[Xe4f^{14}]5s^25p^66s^15d^5$ (known in the VASP database as W_sv). The exchange-correlation energy is evaluated using the Perdew-Burke-Ernzerhof (PBE) parametrization [89] of the generalized gradient approximation (GGA). The DFT setup is exactly the same as in the original dataset from Ref. [48]. In this paper, the training database is composed of the MD-generated configurations and the original database of the previous LML and QNML potentials [48].

The present kernel potential is built on the following two assumptions. The first one is related to the notion of the

empirical potential itself, which states that the total energy E_s of a system s containing N_s atoms can be written as the sum of the local atomic energies $\epsilon_{s,a}$ of each ath atom, $E_s = \sum_{a \in s} \epsilon_{s,a}$. The second one is related to the kernel noise machine learning (KNML) potential, a formalism proposed by the MILADY framework. The KNML model has the same foundation as the QNML framework [48]: Instead of performing a single regression with a fully nonlinear formalism in descriptor space, the linear model (LML) is fitted first and then the kernel model (KML), more difficult to fit, is applied to the difference between the target value and the LML estimation. The model can be written as

$$\epsilon_{s,a}^{\text{KNML}} = \epsilon_{s,a}^{\text{LML}} + \epsilon_{s,a}^{\text{KML}}, \tag{37}$$

$$\epsilon_{s,a}^{\text{KNML}} = (\mathbf{w}^{\text{LML}})^\top \mathbf{D}_{s,a} + (\mathbf{w}^{\text{KML}})^\top \mathbf{k}(\mathbf{D}_{s,a})$$
$$= (\mathbf{w}^{\text{LML}} \oplus \mathbf{w}^{\text{KML}})^\top [\mathbf{D}_{s,a} \oplus \mathbf{k}(\mathbf{D}_{s,a})] \tag{38}$$

where $\mathbf{D}_{s,a}$ is a D-dimensional descriptor that encodes the local neighboring information of the ath atom from the system s within a cutoff distance R_c. Here we use the bispectrum SO(4) descriptor [90] with $D = 55$, $R_c = 5.0$ Å and the angular moment $j_{\max} = 4$. Besides, $\mathbf{k}(\cdot) \in \mathbb{R}^{K \times 1}$ is a column vector that measures the distance in the descriptor space between the descriptor $\mathbf{D}_{s,a} \in \mathbb{R}^D$ and the K sparse points $\mathbf{z}_k \in \mathbb{R}^D$ ($k = 1, \ldots, K$) selected from the database:

$$\mathbf{k}(\mathbf{D}_{s,a}) = \begin{pmatrix} k(\mathbf{D}_{s,a}, \mathbf{z}_1) \\ k(\mathbf{D}_{s,a}, \mathbf{z}_2) \\ \vdots \\ k(\mathbf{D}_{s,a}, \mathbf{z}_K) \end{pmatrix} \in \mathbb{R}^{K \times 1} \tag{39}$$

where $k(\cdot, \cdot) : \mathbb{R}^D \times \mathbb{R}^D \to \mathbb{R}$ is the kernel function. Within this formulation, the LML and KML parts are in direct product $\mathbf{w} = \mathbf{w}^{\text{LML}} \oplus \mathbf{w}^{\text{KML}}$, meaning that there are $1 + D + K$ parameters in total. This can be interpreted as an extension of K components to the original D-dimensional descriptor space. The energy descriptor becomes $\sum_{a \in s} [\mathbf{D}_{s,a} \oplus \mathbf{k}(\mathbf{D}_{s,a})]$, from which the forces and stresses can be derived [45,72,86].

In the present paper we use the normalized polynomial kernel [45,91,92]:

$$k(\mathbf{D}_{s,a}, \mathbf{z}_k) = \frac{\tilde{k}(\mathbf{D}_{s,a}, \mathbf{z}_k)}{\sqrt{\tilde{k}(\mathbf{D}_{s,a}, \mathbf{D}_{s,a})} \sqrt{\tilde{k}(\mathbf{z}_k, \mathbf{z}_k)}},$$

$$\tilde{k}(\mathbf{D}_{s,a}, \mathbf{z}_k) = \left(\sigma^2 + \frac{\mathbf{D}_{s,a} \cdot \mathbf{z}_k}{2l^2} \right)^p. \tag{40}$$

Here σ, l, and p are the kernel hyperparameters. In the KNML framework $\sigma = 0$ because after the linear fitting, the difference between the DFT target values and the LML prediction follows a normal distribution with zero mean [48]. After many trials the other two hyperparameters are set to $l = 0.05$ and $p = 4$. The $K = 3615$ sparse points $\mathbf{z}_k \in \mathbb{R}^D$ are selected via sampling the Mahalanobis distance of the fitting database. We compute the statistical distance of each local atomic descriptor $\mathbf{D}_{s,a}$ for all atoms of the database that contains in total $M = 47\,277$ data points. The Mahalanobis distance of the mth local atomic environment with respect to the covariance matrix $\mathbf{\Sigma} \in \mathbb{R}^{D \times D}$ of all M local descriptors contained in

the database can be written as

$$d(\mathbf{D}_m) = [(\mathbf{D}_m - \boldsymbol{\mu})^\top \mathbf{\Sigma}^{-1} (\mathbf{D}_m - \boldsymbol{\mu})]^{\frac{1}{2}},$$

$$\mathbf{\Sigma} = \frac{1}{M-1} \sum_{m=1}^{M} (\mathbf{D}_m - \boldsymbol{\mu})(\mathbf{D}_m - \boldsymbol{\mu})^\top,$$

$$\boldsymbol{\mu} = \frac{1}{M} \sum_{m=1}^{M} \mathbf{D}_m. \tag{41}$$

The statistical distance $d(\mathbf{D}_m)$ for each point is computed to measure the distance between this point and the distribution of the whole database. Instead of directly sampling the statistical distance $d(\mathbf{D}_m)$, we sample $d^p(\mathbf{D}_m)$ with a very low power p, here equal to 0.05. Then the interval $I_D = [\min_m[d^p(\mathbf{D}_m)], \max_m[d^p(\mathbf{D}_p)]]$ is equally divided into n_K segments, and one point is selected as kernel sparse point in each subinterval if possible. First, from the entire database, for which $M = 47\,277$, $K = 2812$ sparse points are collected from $n_K = 4000$ subintervals of I_D.

Second, we make another dense selection, in addition to the previous one, in the portion of the descriptor space that represents the primarily important components of the database for the physics of our paper. In our case, since we intend to have good elastic constants at high temperatures, we intensify the collection of the configurations related to elastic deformations and finite-temperature MD simulations. Consequently, we perform the same procedure only for three special classes of the database, including the bulk systems under elastic deformations at 0 K, and the perfect bulk systems sampled from MD simulations at 300 and 3000 K [48]. From those classes consisting of 5142 data points we extract 803 sparse points from 1000 subintervals.

Using the above KNML formalism and the fourth-order polynomial kernel, we train a new potential on the new database oriented towards high-temperature properties of bcc W. The present KNML potential is validated by giving almost the same results at reasonable low temperatures (<2000 K) as the GAP (Fig. 9), which is also based on the fourth-order polynomial kernel. The difference between the results of KNML and of GAP, especially at high temperatures, is reasonable as well in consideration of the difference in database, selection of sparse points, and fitting. In terms of computational speed, our KNML potential offers a sixfold increase over GAP potential. Gratifyingly, the predictive ability of the KNML potential is satisfying. All the properties computed with this potential (Fig. 9) are in excellent agreement with the experimental curves. The lattice expansion in Fig. 9(a) closely follows the experimental value up to the melting point. This fact is surprising because the present formulation does not take into account the electronic entropy. Perhaps, the present agreement does not exclude an error compensation in the estimation within GGA-PBE exchange-correlation functional, i.e., the finite-temperature effects are enhanced with the same quantity as the electronic free energy.

Slight disagreement is observed for all elastic constants at temperatures below the Debye temperature of W. This behavior is normal because our free energy calculation method BABF-HA-SVD is based on classical mechanics statics and cannot account for the quantized zero point energy of phonons

in bcc W. This paper focuses on the high-temperature properties of bcc W, while the measurable impact of quantized phonons at low temperature has been investigated in a large amount of recent studies [93–95].

At the intermediate temperature between 1000 and 2000 K, a discrepancy in bulk modulus between the experimental observation and the present KNML potential-based calculation can also be observed. However, this difference is lower than the 0-K difference between the bulk modulus value from the DFT GGA-PBE approach (304.5 GPa) [48] and the

low-temperature experimental value (314.73 GPa) [49]. The overall consistency between the experimental measurements and the present computational results is remarkable in terms of the temperature dependence of the elastic properties, which provides a perspective on the contribution of electronic entropies and the role of exchange-correlation functional.

Based on the results calculated with the accurate KNML potential, a polynomial model is proposed for the rescaled isothermal bulk moduli and elastic constants of bcc W from 0 K to the melting temperature:

$$\frac{B^T(T)}{B^T(T_{\text{Debye}})} = -4.434 \times 10^{-12}T^3 - 2.082 \times 10^{-9}T^2 - 4.042 \times 10^{-5}T + 1.013, \tag{42}$$

$$\frac{C_{11}^T(T)}{C_{11}^T(T_{\text{Debye}})} = -3.018 \times 10^{-13}T^3 - 2.209 \times 10^{-8}T^2 - 6.875 \times 10^{-5}T + 1.029, \tag{43}$$

$$\frac{C'^T(T)}{C'^T(T_{\text{Debye}})} = 5.800 \times 10^{-12}T^3 - 5.166 \times 10^{-8}T^2 - 1.103 \times 10^{-4}T + 1.054, \tag{44}$$

$$\frac{C_{44}^T(T)}{C_{44}^T(T_{\text{Debye}})} = -2.592 \times 10^{-12}T^3 - 1.343 \times 10^{-10}T^2 - 6.616 \times 10^{-5}T + 1.026. \tag{45}$$

This model with proven correctness could be useful to predict the elastic behaviors of bcc W at extremely high temperature which cannot be reached by the experiments.

To briefly summarize the work in this section, we present the overall process of ML potential improvement based on BABF-HA-SVD in conjunction with experimental observations. As a remedy for the high numerical cost of ML force fields, the fast BABF-HA-SVD assessment makes it possible to establish the optimization strategy rapidly.

IV. CONCLUSION

In this paper, we propose and implement an accelerated Bayesian ABF method for sampling the minima of an energy landscape and estimating its free energy. The procedure, developed in the ABF Bayesian-reasoning framework, consists in performing a thermodynamic integration from a reference system, which in the present paper corresponds either to Einstein approximation or to the harmonic approximation, i.e., the second-order Taylor expansion around the energy minimum. We provide two improvements that drastically facilitate the Bayesian sampling. First, we eliminate the numerical instabilities in the harmonic potential energy using a SVD-based filter. This improves the numerical stability of Bayesian sampling, making it feasible and offering systematic character in the free energy exploration. Second, we propose a procedure that introduces weights in the sampling of the mean biasing force from molecular dynamics flow. The use of a simple weighting procedure enhances the sampling efficiency by three orders of magnitude, in terms of speed of convergence towards uniform sampling which is here measured by the Kullback-Leibler divergence. It also yields reliable results two orders of magnitude faster than a traditional MD simulation does.

Beyond the computational efficiency, the present formulation offers two main advantages with respect to the standard TI methods. First, the expectation form of Bayes formula

which serves to construct the mean-force estimator owing to the ergodic theorem can also be used to estimate many other observables, such as elastic dipole tensors and formation volumes. One simply has to replace the potential gradient in Eq. (15) with the desired quantity. Second, the robustness of thermodynamic integration is increased owing to the Bayesian mixing of the target and reference Hamiltonian systems. To illustrate this point, let us consider some defects located in some metastable minima surrounded by very small barriers, e.g., screw dislocations in bcc metals, mobile dislocations loops such as the cluster formed by crowdion interstitial atoms (of $\langle 100 \rangle$ and $\langle 111 \rangle$ types in fcc and bcc crystal, respectively), etc. For these defects, the traditional TI methods are difficult to set up and often fail to sample the free energy basin of interest. Because the sampled distribution for ζ close to 1 mainly reflects the target system, the dynamics may very easily escape from the local energy minimum and introduce transitions with hysteresis along the integration path from $\zeta = 0$ to 1. The ability of the adaptive Bayesian approach to explore rugged energy surfaces opens up many perspectives involving the characterization of complex defects in materials science. In addition to that, the adaptive Bayesian method can be applied for computing free energy of melting in metallic systems. In this case, to evaluate the melting point of the material, an appropriate reference system of liquid, such as the inverse-power pair potential [8], should be provided.

The outstanding performance of the method developed here enables many possibilities for numerical applications. For example, it is well suited to the accurate computation of the free energy landscape and its derived quantities for physical systems described by faithful but time-consuming ML potentials: We prove this for the experimental elastic properties of W, which can be reliably predicted in tens of minutes. Using the Bayesian ABF sampling with linear, quadratic, and kernel ML potentials, we highlight the agreement with the extrapolation laws used for the bcc W thermoelastic properties

obtained by Wang and Reeber [53], and slight disagreement with those obtained by Saxena and Zhang [54]. Our robust Bayesian ABF approach based on kernel ML potential validates only the former ones [53]. Besides, it eventually provides its own extrapolation laws based on the estimated vibrational free energies.

As a final point, being numerically fast and stable, the present free energy method opens up the prospect of new machine/deep learning force-field calibration strategies. Our Bayesian ABF method can (i) significantly accelerate the evaluation of recent machine/deep learning models, potentially revealing deficiencies in the model or database, as well as (ii) indicate the direction of optimization, and (iii) ensure robust evaluation of the free energy within complex FEP workflows dedicated to *ab initio* computations (many of them mentioned in the Introduction).

The MILADY package is open source software under ASL license and can be downloaded from Ref. [96]. The KNML potential developed in this paper is provided on the same webpage. The W database is available upon reasonable request.

[1] N. W. Ashcroft and N. D. Mermin, *Solid State Physics*, Science: Physics (Saunders, Philadelphia, 1976).

[2] J. Rickman and R. LeSar, Annu. Rev. Mater. Res. **32**, 195 (2002).

[3] E. B. Tadmor and R. E. Miller, *Modeling Materials: Continuum, Atomistic and Multiscale Techniques* (Cambridge University, New York, 2011).

[4] A. Glensk, B. Grabowski, T. Hickel, and J. Neugebauer, Phys. Rev. Lett. **114**, 195901 (2015).

[5] T. D. Swinburne, J. Janssen, M. Todorova, G. Simpson, P. Plechac, M. Luskin, and J. Neugebauer, Phys. Rev. B **102**, 100101(R) (2020).

[6] J. G. Kirkwood, J. Chem. Phys. **3**, 300 (1935).

[7] D. Frenkel and B. Smit, *Understanding Molecular Simulation: From Algorithms to Applications* (Elsevier, Amsterdam, 2001), Vol. 1.

[8] D. Alfè, G. D. Price, and M. J. Gillan, Phys. Rev. B **64**, 045123 (2001).

[9] L. Vočadlo and D. Alfè, Phys. Rev. B **65**, 214105 (2002).

[10] B. Grabowski, Y. Ikeda, P. Srinivasan, F. Körmann, C. Freysoldt, A. I. Duff, A. Shapeev, and J. Neugebauer, npj Comput. Mater. **5**, 1 (2019).

[11] B. Grabowski, L. Ismer, T. Hickel, and J. Neugebauer, Phys. Rev. B **79**, 134106 (2009).

[12] A. I. Duff, T. Davey, D. Korbmacher, A. Glensk, B. Grabowski, J. Neugebauer, and M. W. Finnis, Phys. Rev. B **91**, 214311 (2015).

[13] A. V. Shapeev, Multiscale Model. & Simul. **14**, 1153 (2016).

[14] A. Forslund and A. Ruban, Phys. Rev. B **105**, 045403 (2022).

[15] J. H. Jung, P. Srinivasan, A. Forslund, and B. Grabowski, npj Comput. Mater. **9**, 3 (2023).

[16] C. Chipot and A. Pohorille, *Free Energy Calculations* (Springer-Verlag, Berlin, 2007).

[17] E. Darve and A. Pohorille, J. Chem. Phys. **115**, 9169 (2001).

[18] E. Darve, M. A. Wilson, and A. Pohorille, Mol. Simul. **28**, 113 (2002).

[19] F. Wang and D. P. Landau, Phys. Rev. E **64**, 056101 (2001).

[20] F. Wang and D. P. Landau, Phys. Rev. Lett. **86**, 2050 (2001).

[21] T. Huber, A. E. Torda, and W. F. Van Gunsteren, J. Comput. Aided Mol. Des. **8**, 695 (1994).

[22] A. Laio and M. Parrinello, Proc. Natl. Acad. Sci. USA **99**, 12562 (2002).

[23] A. Barducci, G. Bussi, and M. Parrinello, Phys. Rev. Lett. **100**, 020603 (2008).

[24] A. Barducci, M. Bonomi, and M. Parrinello, Wiley Interdiscip. Rev. Comput. Mol. Sci. **1**, 826 (2011).

[25] C. Abrams and G. Bussi, Entropy **16**, 163 (2013).

[26] C. H. Bennett, J. Comput. Phys. **22**, 245 (1976).

[27] G. M. Torrie and J. P. Valleau, J. Comput. Phys. **23**, 187 (1977).

[28] J. Kästner, Wiley Interdiscip. Rev. Comput. Mol. Sci. **1**, 932 (2011).

[29] J. Hénin and C. Chipot, J. Chem. Phys. **121**, 2904 (2004).

[30] E. Darve, D. Rodríguez-Gómez, and A. Pohorille, J. Chem. Phys. **128**, 144120 (2008).

[31] J. Comer, J. C. Gumbart, J. Henin, T. Lelièvre, A. Pohorille, and C. Chipot, J. Phys. Chem. B **119**, 1129 (2015).

[32] L. Cao, G. Stoltz, T. Lelièvre, M.-C. Marinica, and M. Athènes, J. Chem. Phys. **140**, 104108 (2014).

[33] P. Terrier, M.-C. Marinica, and M. Athènes, J. Chem. Phys. **143**, 134121 (2015).

[34] M. Athènes and P. Terrier, J. Chem. Phys. **146**, 194101 (2017).

[35] J. Baima, A. M. Goryaeva, T. D. Swinburne, J.-B. Maillet, M. Nastar, and M.-C. Marinica, Phys. Chem. Chem. Phys. **24**, 23152 (2022).

[36] T. Lelièvre, M. Rousset, and G. Stoltz, J. Chem. Phys. **126**, 134111 (2007).

[37] L. Zheng, M. Chen, and W. Yang, Proc. Natl. Acad. Sci. USA **105**, 20227 (2008).

[38] H. Fu, X. Shao, C. Chipot, and W. Cai, J. Chem. Theory Comput. **12**, 3506 (2016).

[39] L. Mones, N. Bernstein, and G. Csányi, J. Chem. Theory Comput. **12**, 5100 (2016).

[40] A. Lesage, T. Lelièvre, G. Stoltz, and J. Hénin, J. Phys. Chem. B **121**, 3676 (2017).

[41] A. Z. Guo, E. Sevgen, H. Sidky, J. K. Whitmer, J. A. Hubbell, and J. J. de Pablo, J. Chem. Phys. **148**, 134108 (2018).

[42] T. Lelièvre, M. Rousset, and G. Stoltz, Nonlinearity **21**, 1155 (2008).

[43] R. A. Causey and T. J. Venhaus, Phys. Scr. **T94**, 9 (2001).

[44] J. V. Vas, J. Pan, N. Wang, J. Xu, R. Medwal, M. Mishra, J. Y. Pae, M. V. Matham, L. Paul, and R. S. Rawat, J. Mater. Sci. **56**, 10494 (2021).

[45] A. P. Bartók, S. De, C. Poelking, N. Bernstein, J. R. Kermode, G. Csányi, and M. Ceriotti, Sci. Adv. **3**, e1701816 (2017).

[46] V. L. Deringer, M. A. Caro, and G. Csányi, Adv. Mater. **31**, 1902765 (2019).

[47] V. L. Deringer, A. P. Bartók, N. Bernstein, D. M. Wilkins, M. Ceriotti, and G. Csányi, Chem. Rev. **121**, 10073 (2021).

[48] A. M. Goryaeva, J. Dérès, C. Lapointe, P. Grigorev, T. D. Swinburne, J. R. Kermode, L. Ventelon, J. Baima, and M.-C. Marinica, Phys. Rev. Mater. **5**, 103803 (2021).

[49] J. H. Stathis and D. Bolef, J. Appl. Phys. **51**, 4770 (1980).

[50] D. I. Bolef and J. De Klerk, J. Appl. Phys. **33**, 2311 (1962).

[51] F. H. Featherston and J. R. Neighbours, Phys. Rev. **130**, 1324 (1963).

[52] R. Lowrie and A. M. Gonas, J. Appl. Phys. **38**, 4505 (1967).

[53] K. Wang and R. R. Reeber, High Temp. Mater. Sci. **36** (1996).

[54] S. Saxena and J. Zhang, Phys. Chem. Miner. **17**, 45 (1990).

[55] T. Lelièvre, G. Stoltz, and M. Rousset, *Free Energy Computations: A Mathematical Perspective* (Imperial College, London, 2010).

[56] M. Watanabe and W. P. Reinhardt, Phys. Rev. Lett. **65**, 3301 (1990).

[57] W. G. Hoover and F. H. Ree, J. Chem. Phys. **47**, 4873 (1967).

[58] P. A. Monson and D. A. Kofke, Solid-fluid equilibrium: Insights from simple molecular models, in *Advances in Chemical Physics* (Wiley, New York, 2007), p. 113.

[59] W. G. Hoover, M. Ross, K. W. Johnson, D. Henderson, J. A. Barker, and B. C. Brown, J. Chem. Phys. **52**, 4931 (1970).

[60] W. G. Hoover, S. G. Gray, and K. W. Johnson, J. Chem. Phys. **55**, 1128 (1971).

[61] D. Frenkel and A. J. C. Ladd, J. Chem. Phys. **81**, 3188 (1984).

[62] S. Fukushima, E. Ushijima, H. Kumazoe, A. Koura, F. Shimojo, K. Shimamura, M. Misawa, R. K. Kalia, A. Nakano, and P. Vashishta, Phys. Rev. B **100**, 214108 (2019).

[63] B. Grabowski, T. Hickel, and J. Neugebauer, Phys. Status Solidi B **248**, 1295 (2011).

[64] B. Cheng and M. Ceriotti, Phys. Rev. B **97**, 054102 (2018).

[65] L. G. Wang, A. van de Walle, and D. Alfè, Phys. Rev. B **84**, 092102 (2011).

[66] J. Q. Broughton and G. H. Gilmer, J. Chem. Phys. **79**, 5095 (1983).

[67] J. P. Ryckaert and G. Ciccotti, J. Chem. Phys. **78**, 7368 (1983).

[68] M.-C. Marinica, L. Ventelon, M. Gilbert, L. Proville, S. Dudarev, J. Marian, G. Bencteux, and F. Willaime, J. Phys.: Cond. Matter **25**, 395502 (2013).

[69] G. Clavier, N. Desbiens, E. Bourasseau, V. Lachet, N. Brusselle-Dupend, and B. Rousseau, Mol. Simul. **43**, 1413 (2017).

[70] S. Plimpton, J. Comput. Phys. **117**, 1 (1995).

[71] C. Kittel, *Introduction to Solid State Physics* (Wiley, New York, 2004).

[72] A. P. Bartók, M. C. Payne, R. Kondor, and G. Csányi, Phys. Rev. Lett. **104**, 136403 (2010).

[73] J. Behler, J. Chem. Phys. **145**, 170901 (2016).

[74] A. M. Miksch, T. Morawietz, J. Kästner, A. Urban, and N. Artrith, Mach. Learn.: Sci. Technol. **2**, 031001 (2021).

[75] Y. S. Touloukian and E. H. Buyco, *Specific Heat Metallic Elements and Alloys* (Springer US, 1970), Vol. 4.

[76] Y. S. Touloukian, R. K. Kirby, R. E. Taylor, and P. D. Desai, *Thermal Expansion Metallic Elements and Alloys* (Springer US, 1975), Vol. 12.

[77] P. Varotsos and K. Alexopoulos, Phys. Rev. B **22**, 3130 (1980).

[78] C. Falter and W. Zierau, J. Appl. Phys. **51**, 2070 (1980).

[79] P. Gustafson, Int. J. Thermophys. **6**, 395 (1985).

[80] P. M. Derlet, D. Nguyen-Manh, and S. L. Dudarev, Phys. Rev. B **76**, 054107 (2007).

[81] N. Juslin and B. D. Wirth, J. Nucl. Mater. **432**, 61 (2013).

[82] D. R. Mason, D. Nguyen-Manh, and C. S. Becquart, J. Phys.: Condens. Matter **29**, 505501 (2017).

[83] L. Ventelon, F. Willaime, C.-C. Fu, M. Heran, and I. Ginoux, J. Nucl. Mater. **425**, 16 (2012).

[84] W. J. Szlachta, A. P. Bartók, and G. Csányi, Phys. Rev. B **90**, 104108 (2014).

[85] J. Byggmästar, A. Hamedani, K. Nordlund, and F. Djurabekova, Phys. Rev. B **100**, 144105 (2019).

[86] A. M. Goryaeva, J.-B. Maillet, and M.-C. Marinica, Comput. Mater. Sci. **166**, 200 (2019).

[87] X. Wang, Y. Wang, L. Zhang, F. Dai, and H. Wang, Nucl. Fusion **62**, 126013 (2022).

[88] G. Kresse and J. Furthmüller, Phys. Rev. B **54**, 11169 (1996).

[89] J. P. Perdew, K. Burke, and M. Ernzerhof, Phys. Rev. Lett. **77**, 3865 (1996).

[90] A. P. Bartók, R. Kondor, and G. Csányi, Phys. Rev. B **87**, 184115 (2013).

[91] C. E. Rasmussen, *Gaussian Processes in Machine Learning* (Springer-Verlag, Berlin, 2004).

[92] C. C. Aggarwal, *Neural Networks and Deep Learning* (Springer-Verlag, Berlin, 2018).

[93] L. Proville, D. Rodney, and M.-C. Marinica, Nat. Mater. **11**, 845 (2012).

[94] T. D. Swinburne, P.-W. Ma, and S. L. Dudarev, New J. Phys. **19**, 073024 (2017).

[95] K. Arakawa, M.-C. Marinica, S. Fitzgerald, L. Proville, D. Nguyen-Manh, S. L. Dudarev, P.-W. Ma, T. D. Swinburne, A. M. Goryaeva, T. Yamada, T. Amino, S. Arai, Y. Yamamoto, K. Higuchi, N. Tanaka, H. Yasuda, T. Yasuda, and H. Mori, Nat. Mater. **19**, 508 (2020).

[96] https://ai-atoms.github.io/milady/.